

Article

Research on the Thermal Runaway Behavior and Flammability Limits of Sodium-Ion and Lithium-Ion Batteries

Changbao Qi ^{1,2}, Hewu Wang ^{2,*}, Minghai Li ^{1,*}, Cheng Li ², Yalun Li ², Chao Shi ^{1,2}, Ningning Wei ¹, Yan Wang ³ and Huipeng Zhang ⁴

¹ College of Zhan Tianyou, Dalian Jiaotong University, Dalian 116028, China; 1707@sdp.edu.cn (C.Q.); 1716@sdp.edu.cn (N.W.)

² State Key Laboratory of Intelligent Green Vehicle and Mobility, Tsinghua University, Beijing 100084, China

³ School of Mechanical and Automotive Engineering, Qingdao University of Technology, Qingdao 266520, China; wangyan2387@163.com

⁴ Department of Mechanical and Electronic Engineering, Yuncheng University, Yuncheng 044000, China

* Correspondence: wanghw@tsinghua.edu.cn (H.W.); dlmMINGhai8813@djtu.edu.cn (M.L.)

Abstract: Batteries are widely used in energy storage systems (ESS), and thermal runaway in different types of batteries presents varying safety risks. Therefore, comparative research on the thermal runaway behaviors of various batteries is essential. This study investigates the thermal runaway characteristics of sodium-ion batteries (NIBs), lithium iron phosphate batteries (LFP), and lithium-ion batteries with NCM523 and NCM622 cathodes. The experiments were conducted in a nitrogen-filled constant-volume sealed chamber. The results show that the critical surface temperatures at the time of thermal runaway are as follows: LFP (346 °C) > NIBs (292 °C) > NCM523 (290 °C) > NCM622 (281 °C), with LFP batteries exhibiting the highest thermal runaway critical temperature. NIBs have the lowest thermal runaway triggering energy (158 kJ), while LFP has the highest (592.8 kJ). During the thermal runaway of all four battery types, the primary gases produced include carbon dioxide, hydrogen, carbon monoxide, methane, ethylene, propylene, and ethane. For NCM622 and NCM523, carbon monoxide is the dominant combustible gas, with volume fractions of 35% and 29%, respectively. In contrast, hydrogen is the main flammable gas for LFP and NIBs, with volume fractions of 44% and 30%, respectively. Among these, NIBs have the lowest lower flammability limit (LFL), indicating the highest explosion risk. The thermal runaway characteristics of 50 Ah batteries provide valuable insights for battery selection and design in energy storage applications.

Keywords: lithium-ion batteries; sodium-ion batteries; thermal runaway; gas analysis



Academic Editor: Harry E. Hoster

Received: 21 November 2024

Revised: 9 January 2025

Accepted: 10 January 2025

Published: 12 January 2025

Citation: Qi, C.; Wang, H.; Li, M.; Li, C.; Li, Y.; Shi, C.; Wei, N.; Wang, Y.; Zhang, H. Research on the Thermal Runaway Behavior and Flammability Limits of Sodium-Ion and Lithium-Ion Batteries. *Batteries* **2025**, *11*, 24. <https://doi.org/10.3390/batteries11010024>

Copyright: © 2025 by the authors. Licensee MDPI, Basel, Switzerland. This article is an open access article distributed under the terms and conditions of the Creative Commons Attribution (CC BY) license (<https://creativecommons.org/licenses/by/4.0/>).

1. Introduction

The environmental pollution caused by traditional fossil fuels has drawn increasing attention, leading to widespread adoption of clean energy technologies such as batteries in transportation and energy storage fields [1]. Lithium-ion batteries (LIBs), known for their high energy density and long lifespan, have become the most widely used type of battery. However, due to the limited availability of lithium resources in nature and the high cost of material extraction, sodium-ion batteries (NIBs) have emerged as a promising alternative, garnering significant attention. NIBs offer advantages such as abundant sodium resources, low material costs, and environmental friendliness, making them highly suitable for energy storage applications.

Nevertheless, both LIBs and NIBs face the issue of thermal runaway [2]. Thermal runaway refers to the rapid temperature rise within a battery due to external factors such

as mechanical shock, high ambient temperatures, overcharging, or electrode short circuits. This process triggers intense chemical reactions among electrode materials and electrolytes, releasing large amounts of toxic and flammable gases, ultimately leading to combustion, explosion, or other forms of damage, posing severe risks to health and safety. Fire hazards and failures caused by thermal runaway have become a critical constraint limiting the broader application of batteries [3–7].

Significant research has been conducted on the hazards of thermal runaway. Xu et al. studied the gas generation of 50 Ah NCM622 battery modules during thermal runaway using a custom-made sealed container. They found that the primary gases collected after thermal runaway were CO, CO₂, H₂, CH₄, and C₂H₄, with the gas composition varying by the state of charge (SOC): higher SOCs led to lower CO₂ content but higher C₂H₄ and CO levels, while H₂ and CH₄ remained stable [8]. Qi et al. used an Accelerating Rate Calorimeter (ARC) and Gas Chromatography-Mass Spectrometry (GC-MS) to analyze the gas composition of NCM523 batteries at different SOCs, revealing that CO₂ decreased while CO and H₂ increased with higher SOCs [9]. Zou et al. conducted gas generation studies on 78 Ah NCM811 batteries at 0 SOC, 50 SOC, and 100 SOC using a custom pressure vessel and GC-MS. They found that O₂ was not generated at 0 SOC, while 50 SOC produced 0.27% oxygen, and 100 SOC resulted in oxygen depletion in the air, causing CO₂ content to rise. The main gases were CO, CO₂, H₂, CH₄, C₂H₄, and C₂H₆ [10].

Jia et al. studied the thermal runaway behavior and gas generation mechanisms of 86 Ah LiFePO₄ batteries, finding that H₂ and CO were the primary gases, with H₂ diffusing significantly faster than CO [11]. Wang et al. investigated the effects of charge rates on gas generation during LiFePO₄ battery thermal runaway, identifying H₂, CO, CO₂, and various alkane compounds as the main gases, with H₂ levels increasing significantly with higher charge rates [12]. Cui et al. compared the gas compositions of NCM and LFP batteries after thermal runaway and found that LFP batteries produced significantly more H₂, resulting in a higher explosion risk than NCM batteries [13]. Lin et al. studied the flammability upper and lower limits of gases emitted during thermal runaway of lithium iron phosphate (LFP) batteries in different gas atmospheres. The study showed that the LFP battery at 100% SOC exhibits the best safety performance in a nitrogen atmosphere [14].

Bordes et al. analyzed the gas composition of 18650 NIBs during thermal runaway using a non-dispersive infrared (NDIR) analyzer and Fourier-transform infrared (FTIR) spectrometer. They reported that the most abundant component was electrolyte vapor, followed by CO₂, CO, C₂H₄, HF, H₂, and CH₄ [15].

Previous studies have primarily focused on the triggering mechanisms and gas composition analysis of small-capacity LIBs during thermal runaway. However, research on gas generation in large-capacity batteries is limited, and significant capacity differences among battery types can affect gas analysis. This study investigates four types of 50 Ah commercial batteries, including LFP, NCM523, NCM622, and NIBs. Using a sealed experimental chamber filled with nitrogen, thermal runaway was induced by side heating with a heating plate. The study collected data on temperature, voltage, mass loss, and gas pressure during thermal runaway and analyzed the gas composition. The mole fractions of gas components were calculated based on pressure data, and the flammability limits of gas mixtures for each battery type were determined. The main work of this study is to provide a comprehensive evaluation of the thermal runaway characteristics and gas generation explosion hazards of different types of batteries (sodium-ion batteries and lithium-ion batteries) with the same capacity (50 Ah) under lateral heating in a confined space. The findings offer valuable guidance for firefighting strategies for fires involving different types of batteries.

2. Experimental Methodology

2.1. Battery Samples

The experimental subjects are four different types of commercial prismatic batteries, each with a nominal capacity of 50 Ah. Sample 1 has a cathode material of LiFePO₄ and an anode material of graphite; Sample 2 has a cathode material of NaNi_{0.3}Fe_{0.3}Mn_{0.3}O₂ and an anode material of hard carbon; Sample 3 has a cathode material of LiNi_{0.5}Co_{0.2}Mn_{0.3}O₂ and an anode material of graphite; Sample 4 has a cathode material of LiNi_{0.6}Co_{0.2}Mn_{0.2}O₂ and an anode material of graphite. Among the four samples, the battery length is 148 mm for all of them. The thickness of Sample 1 and Sample 2 is the same, both 39.7 mm, while Sample 3 and Sample 4 have the same thickness of 27 mm. The volume of the four samples, from smallest to largest, is as follows: NCM622 < NCM523 < LFP < NIBs. Other information for the four samples is shown in Table 1 below. Each sample was tested twice.

Table 1. Parameters of the Battery Samples Used in the Experiments.

Cell	LFP	NIBs	NCM523	NCM622
Shape	Square	Square	Square	Square
Cathode	LiFePO ₄	NaNi _{0.3} Fe _{0.3} Mn _{0.3} O ₂	LiNi _{0.5} Co _{0.2} Mn _{0.3} O ₂	LiNi _{0.6} Co _{0.2} Mn _{0.2} O ₂
Anode	Graphite	Hard carbon	Graphite	Graphite
Cell dimensiont (mm)	148 × 95.4 × 39.7	148 × 102 × 39.7	148 × 102 × 27	148 × 98 × 27
Specific energy (Wh/kg)	142	130	209	213
Weight (g)	1130	1120	870	860
Upper limit cut-off voltage (V)	3.65	3.9	4.3	4.3
Lower cut-off voltage (V)	2.5	1.5	2.8	2.8
Wrapper material	Al Alloy	Al Alloy	Al Alloy	Al Alloy
Typical capacity (Ah)	50	50	50	50
SO _C (%)	100	100	100	100
Separator	Polyolefins	Polyolefins	Polyolefins	Polyolefins
Main Components of Electrolyte	Carbonate Solvent + Lithium Hexafluorophosphate (LiPF ₆)	Carbonate Solvent + Sodium Hexafluorophosphate (NaPF ₆)	Carbonate Solvent + Lithium Hexafluorophosphate (LiPF ₆)	Carbonate Solvent + Lithium Hexafluorophosphate (LiPF ₆)

2.2. Experimental Instruments

As shown in Figure 1, the primary experimental apparatus used in this study is a custom-made sealed container. The apparatus comprises five main components: a gas-sealed chamber, a data acquisition system, a gas replacement system, a battery heating system, a gas composition analysis system, and the main framework of the equipment.

As depicted in Figure 2, the gas-sealed chamber has a cylindrical structure. The chamber door uses a mechanical locking mechanism, sealed with 11 manually tightened bolts and rubber gaskets. The chamber consists of three layers: an internal metal layer, a middle insulation layer, and an external structural layer. The internal metal layer is made of aluminum alloy, the middle insulation layer uses aluminum silicate material, and the external structural layer is made of carbon steel. The maximum pressure capacity of the chamber is 2.5 MPa. Inside the chamber, an experimental platform is provided to place the battery.

The data acquisition system records pressure data from the gas-sealed chamber, surface temperature data from the battery, and battery voltage data. A pressure sensor with a range of 0–400 kPa and an accuracy of ±0.2% FS is installed on the chamber's side to monitor real-time pressure changes caused by gas generation during battery thermal runaway. The pressure sensor's data is transmitted to a computer for display and storage.

Five K-type armored thermocouples (with a range of –200 °C to 1300 °C) are installed at the bottom of the chamber. These measure the temperatures of the battery's heated side, the non-heated side, and the chamber environment. The thermocouple data is collected and displayed on a computer via a data acquisition instrument. Additionally, voltage

monitoring wires are connected to the battery terminals using alligator clips to measure voltage changes during thermal runaway. The voltage signals are also transmitted to the computer for display and storage.

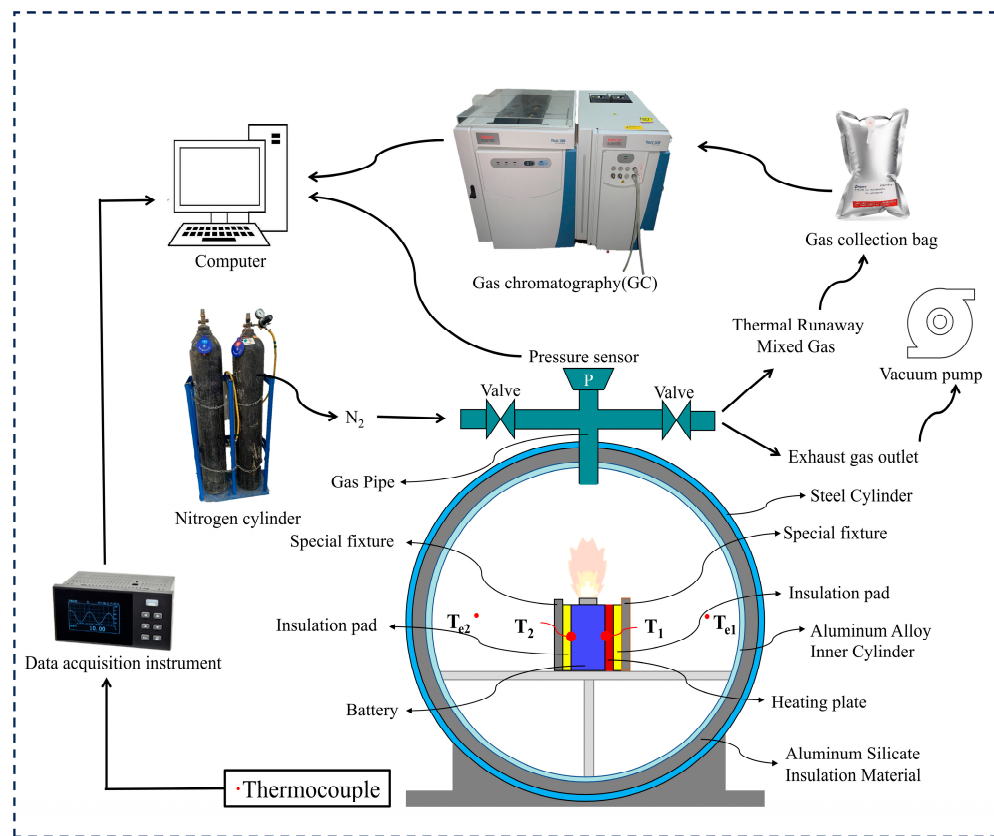


Figure 1. Schematic Diagram of the Experimental Setup.

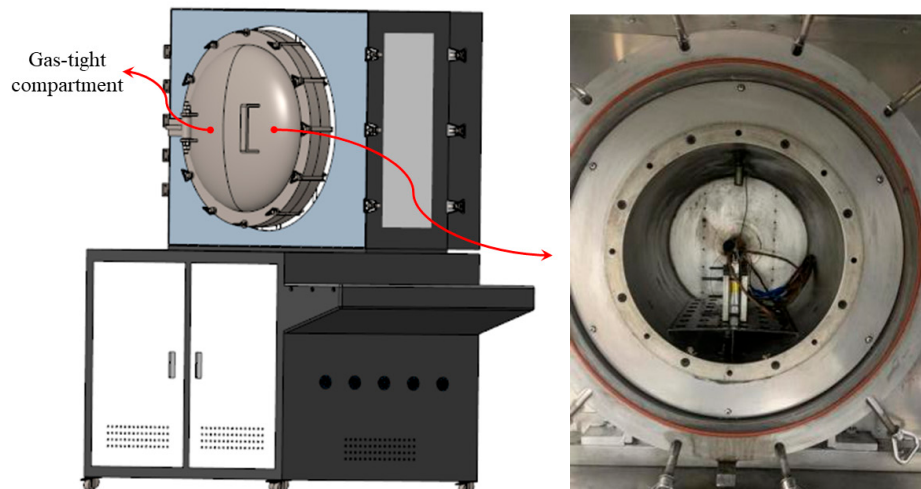


Figure 2. 3D Model and Actual Photograph of the Gas-Sealed Chamber.

The gas replacement system includes a nitrogen cylinder, an intake valve, an exhaust valve, a vacuum pump, and a PLC control system. The nitrogen cylinder supplies nitrogen gas with a purity of 99.9%. The vacuum pump removes the air inside the sealed chamber, creating a vacuum environment. The PLC control system manages the opening and closing of the intake and exhaust valves, ensuring that the air in the chamber is entirely replaced with 99.9% pure nitrogen. All thermal runaway experiments in this study are conducted in a nitrogen atmosphere.

The gas composition analysis system analyzes the gas generated during thermal runaway. The gas mixture is collected in an aluminum foil sampling bag and analyzed using a gas chromatograph (Model: TRACE 1300, Manufacturer: Thermo Fisher Scientific, Country: Singapore). Equipped with four gas detectors and eight chromatographic columns, the system effectively detects the gas components generated during thermal runaway under a nitrogen atmosphere.

The battery heating system uses an electric heating plate (resistance: $91.8\ \Omega$, power: 400 W) to trigger battery thermal runaway. As shown in Figure 3, the heating plate is placed adjacent to the battery's side. Upon powering the heating plate, it generates substantial heat, which is directly transferred to the battery's heated surface, causing the battery to warm up until thermal runaway occurs. To ensure efficient heat transfer, mica insulation boards (thickness: 2 mm) are placed between the battery and the heating plate to isolate heat. The entire assembly is secured with aluminum alloy clamps and bolts.

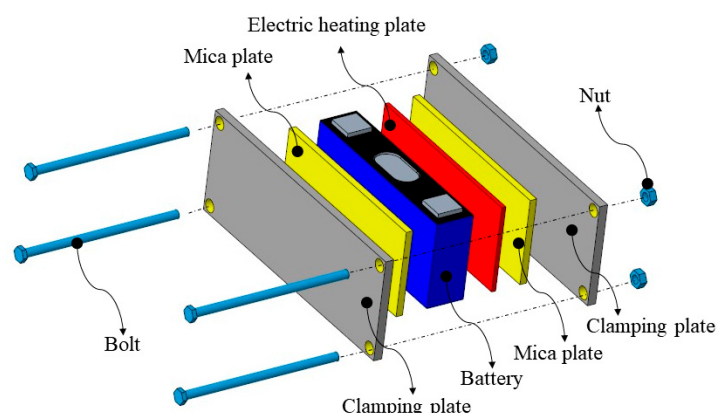


Figure 3. Schematic Diagram of the Battery Side-Heating Fixture.

Figure 4a–h illustrates the pre- and post-thermal runaway states of the four battery types.

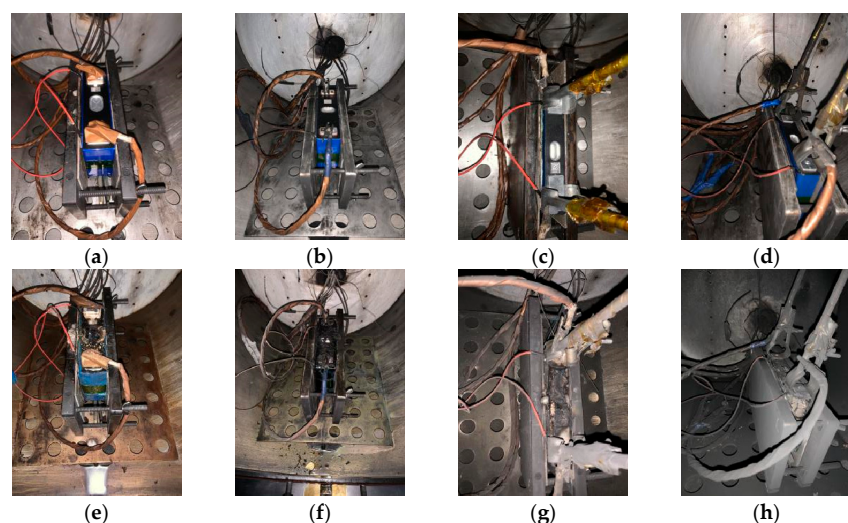


Figure 4. Pre- and Post-Thermal Runaway States of the Four Battery Types. (a) Initial state of the LFP (lithium iron phosphate) battery before the experiment. (b) Initial state of the NIBs (sodium-ion) battery before the experiment. (c) Initial state of the NCM523 (lithium nickel cobalt manganese oxide) battery before the experiment. (d) Initial state of the NCM622 (lithium nickel cobalt manganese oxide) battery before the experiment. (e) Final state of the LFP battery after the experiment. (f) Final state of the NIBs battery after the experiment. (g) Final state of the NCM523 battery after the experiment. (h) Final state of the NCM622 battery after the experiment.

2.3. Experimental Procedure

According to the battery specifications, the four test batteries underwent charge-discharge cycles using the Neware charge-discharge test system (Manufacturer:Neware, Model:CT-4002-5V100A-NA, 2 channels, voltage/current accuracy $\pm 0.1\%$ FS, power accuracy $\pm 0.2\%$ FS, Country:China). Each battery was charged at 1/3C constant current-constant voltage (CC-CV) to the upper cutoff voltage and discharged at 1/3C constant current (CC) to the lower cutoff voltage, repeated three times. The upper and lower cutoff voltages for the batteries are as follows:

- NCM622 and NCM523: Upper voltage 4.3 V, lower voltage 2.8 V
- LFP: Upper voltage 3.65 V, lower voltage 2.5 V
- NIBs: Upper voltage 3.9 V, lower voltage 1.5 V

Finally, the batteries were charged to their upper cutoff voltage (100% SOC) and allowed to rest for 24 h.

The experimental procedure is as follows:

- (a) Open the gas-sealed chamber door and place the battery on the platform inside the chamber. Use Teflon tape to attach one thermocouple (T_f) to the center of the battery's large surface and another thermocouple (T_b) to the center of the back surface. Two additional thermocouples (T_{e1} and T_{e2}) are placed in the chamber environment on either side of the battery to measure ambient temperature.
- (b) Place the electric heating plate on one side of the battery and secure it using Teflon tape. Install two 2 mm mica insulation boards on either side of the battery and fix the setup with two aluminum alloy clamping plates and four bolts. Tighten the bolts to 1 N·m using a torque wrench.
- (c) Close the chamber door and tighten the 11 manual locking bolts with a specialized wrench to ensure airtight sealing.
- (d) Replace the air inside the chamber with nitrogen as follows: (1) Open the exhaust valve and close the intake valve using the PLC control system. Activate the vacuum pump to evacuate the chamber until the relative pressure reaches -90 kPa. (2) Close the exhaust valve, open the intake valve, and fill the chamber with 99.99% pure nitrogen gas until the relative pressure reaches 0 kPa. (3) Repeat steps (1) and (2) three times to reduce the oxygen content inside the chamber to 0.02%.
- (e) Start the data acquisition system on the computer and power on the heating plate. Monitor the voltage, temperature, and pressure data in real-time. When the voltage drops to 0 V, immediately disconnect the power to the heating plate. Thermal runaway will continue, and the battery surface temperature and chamber pressure data will be recorded in real-time.
- (f) After thermal runaway concludes and the battery surface temperature drops below 50 °C, collect the generated gas into an aluminum foil sampling bag via the gas collection pipeline. Analyze the gas composition using gas chromatography-mass spectrometry (GC-MS).
- (g) Open the chamber door and observe the morphology of the battery after thermal runaway. Measure the mass of the remaining battery material using a mass sensor and collect any ejected particles.
- (h) Clean the chamber thoroughly and prepare for the next experiment. A total of four experiments were conducted.

3. Results and Data Analysis

3.1. Temperature and Voltage Changes During Battery Thermal Runaway

Battery thermal runaway was triggered by side-heating the largest surface of the battery using a 400 W electric heating plate. The surface temperature on the heated side (T_f), the surface temperature on the non-heated side (T_b), and the battery voltage were measured and recorded using data acquisition equipment at a frequency of 1 Hz.

The time point at which the battery voltage begins to drop was defined as time zero ($t = 0$). By defining critical temperatures for T_f and T_b , the thermal runaway process of the battery can be segmented and analyzed [16].

As shown in Figure 5a for sodium-ion batteries and Figure 5b for lithium iron phosphate (LFP) batteries, the thermal runaway process can be divided into four stages:

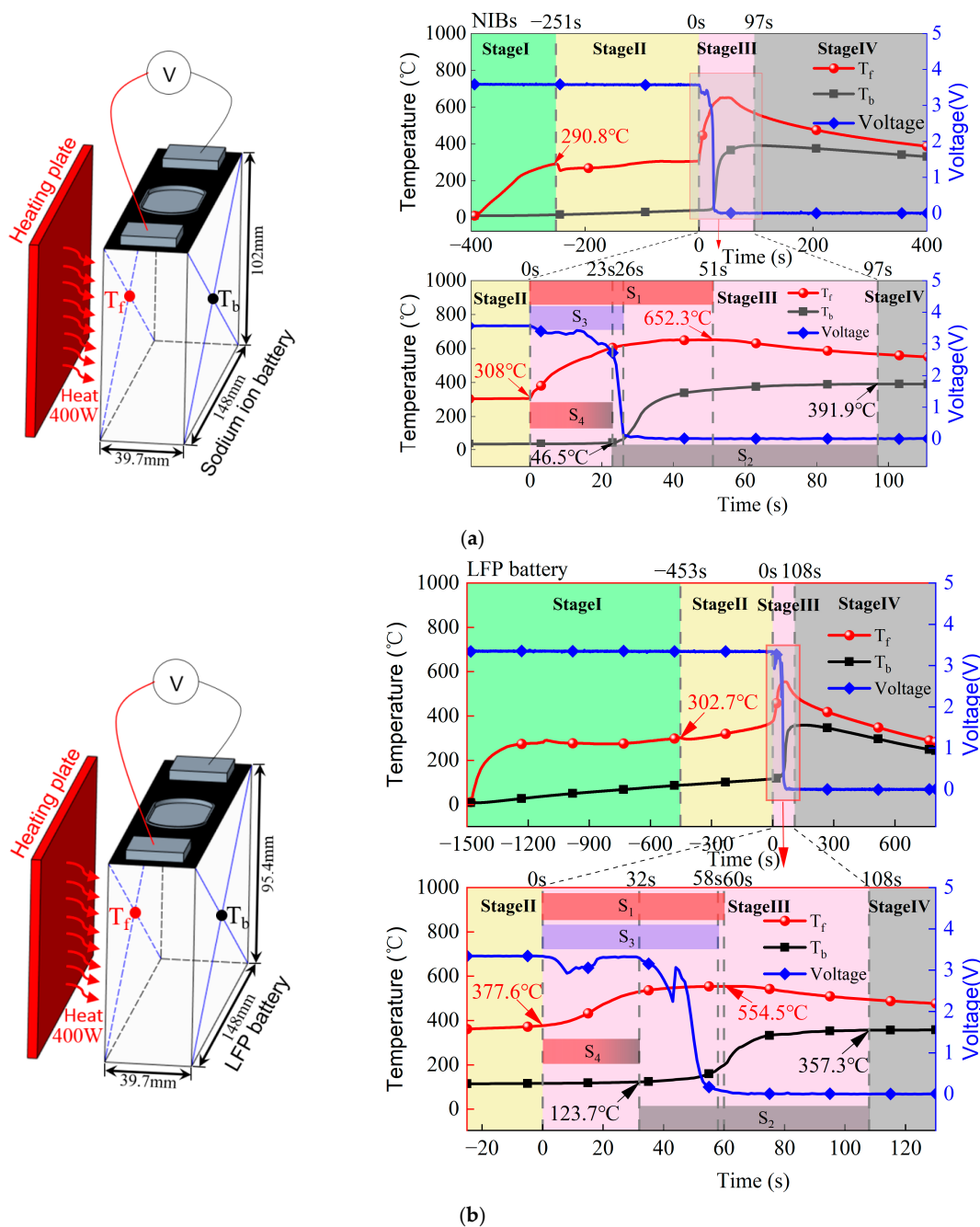


Figure 5. Cont.

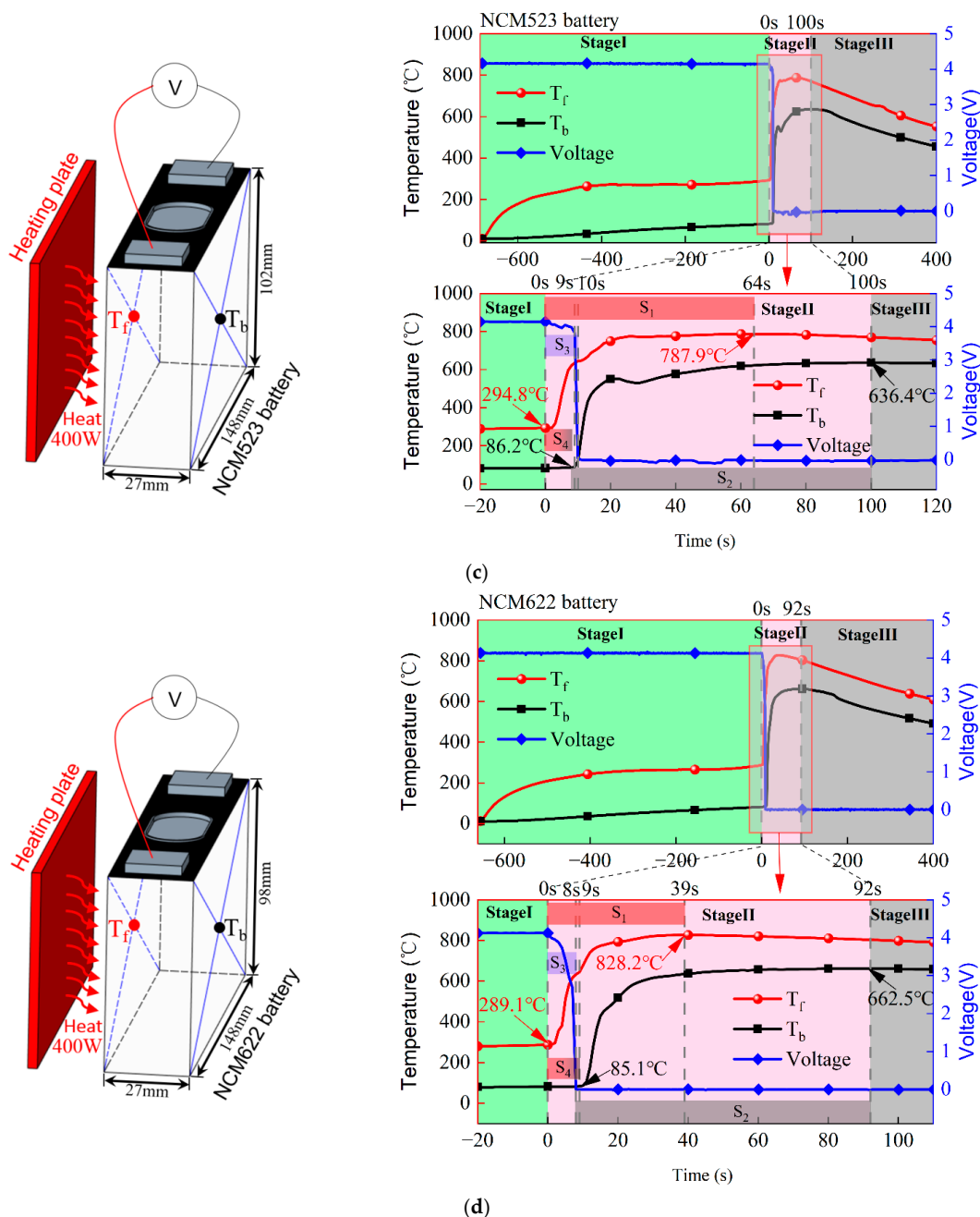


Figure 5. Temperature and Voltage Changes During Thermal Runaway of Four Batteries. (a) Temperature and voltage changes during thermal runaway of NIBs battery; (b) Temperature and voltage changes during thermal runaway of LFP battery; (c) Temperature and voltage changes during thermal runaway of NCM523 battery; (d) Temperature and voltage changes during thermal runaway of NCM622 battery.

Heat Accumulation Stage: This stage spans from the start of heating to the point before the safety valve opens. During this stage, the external heating plate directly contacts the side of the battery, causing the temperature on that side to rise. Heat is gradually transferred from the heated side to the rest of the battery via the cathode, anode, electrolyte, and aluminum alloy shell. The temperature distribution in the battery shows a gradient, with the heated side being hotter. As the temperature increases, internal chemical reactions intensify, generating more heat, accelerating electrolyte evaporation, and causing the internal pressure to approach the critical point for the safety valve to open.

Electrolyte Evaporation Stage: This stage spans from the moment the safety valve opens to the point when the heated-side temperature (T_f) begins to increase rapidly ($\geq 1 \text{ }^{\circ}\text{C/s}$). At this stage, the safety valve opens, releasing a mixture of electrolyte vapor and gases generated from internal chemical reactions into the chamber, where they mix with nitrogen. The separator begins to shrink and melt, increasing the risk of internal short circuits between the cathode and anode.

Violent Thermal Runaway Reaction Stage: This stage spans from the point when T_f begins to rise rapidly to the point when the temperature on the non-heated side (T_b) reaches its peak. As the temperature continues to rise, the separator degrades, and the cathode and anode come into direct contact, leading to internal short circuits within the battery core. This results in the rapid generation of heat and gas, causing the internal pressure to increase sharply. Portions of the separator, electrodes, and thermal runaway reaction products are ejected through the safety valve. The battery's surface temperature reaches its maximum during this stage.

Thermal Runaway Completion Stage: This stage begins after T_b reaches its peak temperature. Following the ejection of materials and gases, internal chemical reactions subside, and the battery's heat generation rate becomes lower than the heat dissipation rate. The battery temperature gradually decreases until it aligns with the ambient temperature.

The point at which the voltage of sodium-ion (NIB) and lithium iron phosphate (LFP) batteries begins to fluctuate coincides with the inflection point of the temperature at the battery heating surface. As the thermal runaway front progresses from the heating surface towards the back of the battery, the voltage continues to fluctuate. For sodium-ion batteries, the voltage fluctuation range is between 3.581 V and 2.72 V, while for lithium iron phosphate batteries, the fluctuation range is between 3.345 V and 2.245 V. During this phase, two voltage peaks are observed for both types of batteries. Once the thermal runaway front reaches the back of the battery, the voltage starts to drop rapidly until it reaches 0 V.

In contrast, for the NCM523 battery (Figure 5c) and the NCM622 battery (Figure 5d), the opening of the safety valve and the onset of the violent thermal runaway reaction occur almost simultaneously, resulting in the process being divided into three stages:

Heat Accumulation Stage: This stage spans from the start of heating to the point before the safety valve opens. The surface temperature of the battery casing increases due to lateral heating, and the heat conduction causes the electrolyte and electrode materials to warm up as well. During this stage, the rate of internal chemical reactions accelerates, generating heat that cannot be quickly dissipated, leading to further temperature increases. Electrolyte evaporation produces a mixture of vapors and gases, increasing the internal pressure without reaching the threshold for the safety valve to open.

Safety Valve Opening and Violent Reaction Stage: This stage spans from the moment the safety valve opens to the point when T_b reaches its peak temperature. Once the temperature and pressure inside the battery reach the safety valve's critical threshold, the valve ruptures, releasing high-temperature, high-pressure gases to prevent the casing from exploding. Despite the pressure relief, the elevated temperature destroys the solid electrolyte interphase (SEI) layer, leading to short circuits between the electrodes. This triggers intense chemical reactions between the electrodes and electrolyte, causing cathode decomposition, electrolyte combustion, and the release of a large volume of flammable gases and solid combustion products.

Thermal Runaway Completion Stage: This stage begins after T_b reaches its peak temperature. Most active chemical substances have reacted by this point, and the battery temperature starts to decline. The heat generation rate during thermal runaway becomes lower than the heat dissipation rate, transitioning the battery into the cooling phase post-thermal runaway.

For the NCM523 battery, the point at which the voltage begins to fluctuate coincides with the inflection point of the temperature at the battery heating surface. As the thermal runaway front progresses from the heating surface towards the back of the battery, the voltage remains fluctuating. The fluctuation range for the NCM523 battery is between 4.147 V and 3.987 V, with one voltage peak observed during this phase. Once the thermal runaway front reaches the back of the battery, the voltage begins to decrease rapidly until it reaches 0 V.

In contrast, for the NCM622 battery, the voltage starts to decrease at the same inflection point of the heating surface temperature. However, throughout the process, until the thermal runaway front reaches the back of the battery, no voltage peaks are observed. The voltage follows a parabolic shape, gradually decreasing until it reaches 0 V.

Through the comparison of the thermal runaway processes of four different battery systems with the same capacity, it was found that the thermal runaway process of NIBs batteries is similar to that of LFP batteries. During the thermal runaway process, as heat accumulates, the safety valve opens, releasing high-temperature mixed gases. After prolonged heating, the battery undergoes a further intense thermal runaway (sharp temperature increase), which is significant for thermal runaway early warning. In contrast, for the two types of NCM lithium batteries, due to their higher energy density, the opening of the safety valve and the intense thermal runaway (sharp temperature rise) occur simultaneously. Therefore, it is almost impossible to use the opening of the safety valve as an early warning indicator for thermal runaway.

Figure 6 presents the surface temperatures of the four battery samples during thermal runaway. In Figure 6a, T_f represents the surface temperature of the battery near the electric heating plate, while T_b represents the surface temperature on the side away from the heating plate. The critical temperature for thermal runaway (T_{f-TR}) of the batteries near the heating plate are as follows: LiFePO₄ (LFP) battery: 346 °C, Sodium-ion battery (NIBs): 292 °C, NCM523 battery: 290 °C, NCM622 battery: 281 °C. Once this critical temperature is exceeded, the battery enters the rapid thermal runaway phase, with the surface temperature of the battery continuing to rise. The thermal runaway initiation critical temperature (T_{f-TR}) can be used to measure the thermal runaway stability of the battery; the higher the temperature, the more stable the battery is. Based on the data, the thermal runaway stability of the four batteries from highest to lowest is as follows: LFP > NIBs > NCM523 > NCM622. The higher thermal runaway initiation critical temperature of the LFP battery is due to the olivine structure of the LiFePO₄ cathode material, which is more stable at high temperatures and is less prone to decomposition. In contrast, sodium-ion cathode materials are less stable at high temperatures, making them more likely to undergo decomposition. Lithium nickel cobalt manganese (NCM) batteries contain highly reactive nickel and cobalt, which are more likely to undergo violent oxidation-reduction reactions at high temperatures.

The critical temperature for the surface away from the heating plate (T_{b-TR}) for the four batteries is as follows: LFP: 117 °C, NIBs: 47.2 °C, NCM523: 79.5 °C, NCM622: 86.8 °C. The LFP battery has the highest critical temperature on this side, indicating that it is more stable than the other batteries. The T_{b-TR} temperature is influenced by several factors, including the activity of the internal materials, the heat generated by the battery, the specific heat capacity, the heat dissipation, and the battery size [17].

$T_{f-\max}$ represents the highest surface temperature near the electric heating plate for the four batteries: LFP: 553 °C, NIBs: 662 °C, NCM523: 798 °C, NCM622: 852 °C. The maximum surface temperature on the side away from the heating plate ($T_{b-\max}$) is as follows: LFP: 361 °C, NIBs: 438 °C, NCM523: 666 °C, NCM622: 683 °C. The maximum temperature during thermal runaway can be used to assess the potential hazard of high temperatures

during thermal runaway. In this study, the temperature trend of both $T_{f\text{-max}}$ and $T_{b\text{-max}}$ is consistent, and the thermal runaway high-temperature hazards of the batteries are ranked as follows: NCM622 > NCM523 > NIBs > LFP. The LFP battery has the lowest $T_{f\text{-max}}$ temperature, which is due to the higher stability of the LiFePO₄ cathode material, which is less likely to react violently with the electrolyte at high temperatures and produces less heat. NCM batteries have the highest temperatures due to the high reactivity of nickel and cobalt, which react violently with the electrolyte at lower temperatures, releasing combustible gases and a large amount of heat, causing the surface temperature of the battery to rise sharply. [18].

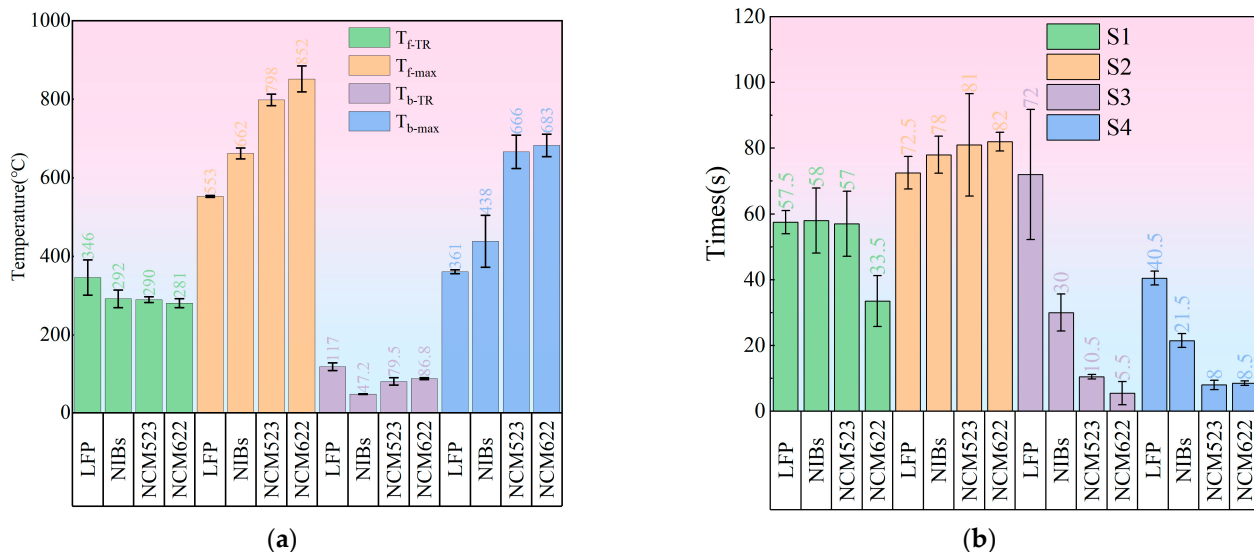


Figure 6. Key Temperature and Time Parameters of Thermal Runaway. **(a)** Key temperature parameters of thermal runaway for the four batteries. **(b)** Key time parameters of thermal runaway for the four batteries. $T_{f\text{-TR}}$: Critical temperature on the side near the heating plate, beyond which the temperature rapidly increases at a rate greater than $1^{\circ}\text{C}/\text{s}$. $T_{f\text{-max}}$: Maximum temperature on the side near the heating plate. $T_{b\text{-TR}}$: Critical temperature on the side away from the heating plate, beyond which the temperature rapidly increases at a rate greater than $1^{\circ}\text{C}/\text{s}$. $T_{b\text{-max}}$: Maximum temperature on the side away from the heating plate. S₁: Duration of rapid temperature increase for T_f , defined as the time from $T_{f\text{-TR}}$ to $T_{f\text{-max}}$. S₂: Duration of rapid temperature increase for T_b , defined as the time from $T_{b\text{-TR}}$ to $T_{b\text{-max}}$. S₃: Duration of voltage change, defined as the time taken for the voltage to drop from its nominal value to 0 V. S₄: Duration of thermal runaway propagation, defined as the time taken for thermal runaway to spread from the front surface of the battery to the back surface.

Figure 6b shows the thermal runaway time parameters for the four batteries. S₁ represents the duration of rapid temperature rise near the heating plate (T_f), from the $T_{f\text{-TR}}$ moment to the $T_{f\text{-max}}$ moment. S₂ represents the duration of rapid temperature rise on the side away from the heating plate (T_b), from the $T_{b\text{-TR}}$ moment to the $T_{b\text{-max}}$ moment. This study found that the battery surface near the heating plate radiates the maximum heat within the range of 33.5–58 s, while the back surface of the battery radiates the maximum heat within the range of 72.5–82 s.

S₃ represents the duration of voltage drop. The duration from the standard voltage to 0 V is as follows: LFP: 72 s, NIBs: 30 s, NCM523: 10.5 s, NCM622: 5.5 s. Therefore, the voltage change duration, from longest to shortest, is: LFP > NIBs > NCM523 > NCM622. The LFP battery has the longest voltage change duration, indicating the least severe thermal runaway. During the thermal runaway process, the temperature distribution of the battery, triggered by side heating, shows a gradient from front to back. As the temperature rises, the solid electrolyte interface (SEI) film inside the battery decomposes, and the cathode

material gradually decomposes and undergoes side reactions, leading to changes in the internal resistance of the battery, causing the voltage to fluctuate. Internal short circuits will eventually lead to a sudden reduction in the battery's internal resistance, and the voltage will drop to 0. Various internal reactions, such as electrolyte decomposition, SEI film rupture, and cathode material decomposition, occur progressively, not simultaneously.

S_4 represents the duration it takes for thermal runaway to spread from the front to the back surface of the battery. It can be seen that the thermal propagation time (S_4) follows a pattern similar to the voltage duration (S_3). The thermal reactivity of the LiFePO₄ cathode material is lower, and the rate of chemical reactions inside the battery is relatively slow at high temperatures. In contrast to the NCM batteries, the thermal runaway of the LiFePO₄ battery does not occur instantaneously but progresses gradually, leading to a more gradual voltage change. The sodium-ion battery is in an intermediate state between the two.

Figure 7a shows the thermal runaway propagation rates within the four batteries. By combining the thickness dimensions of the batteries and the time t_{TR} required for thermal runaway to propagate from the front surface to the back surface, the thermal runaway propagation rates within the batteries can be calculated using Equation (1).

$$v = \frac{L}{t_{TR}} \quad (1)$$

where v represents the thermal runaway propagation rate within the battery, in mm/s; L is the battery thickness, in mm; and t_{TR} is the thermal propagation time within the battery, defined as the duration from the inflection point of the front surface temperature to the inflection point of the back surface temperature, in seconds.

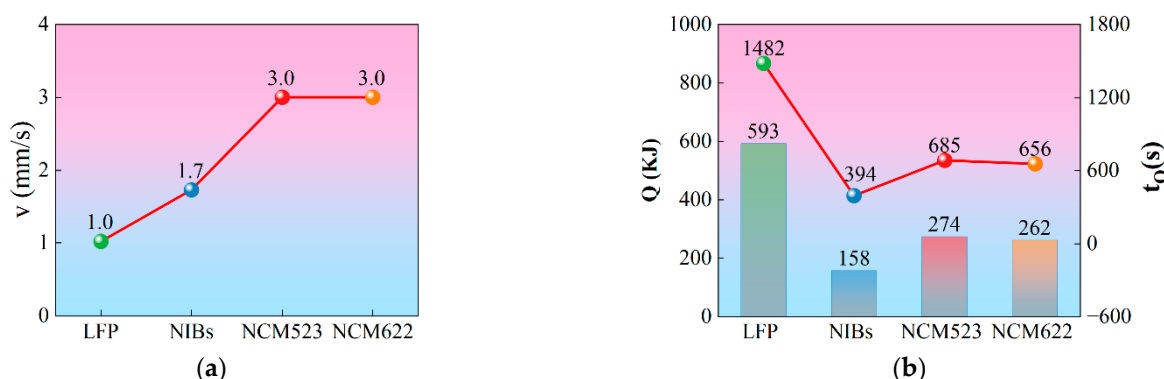


Figure 7. Heat Accumulation and Thermal Runaway Propagation Rate in Batteries. (a) Thermal runaway propagation rates within the four batteries. (b) Heat generated by the heating plate and the duration of heating of the electric heating plate.

Using Equation (1), the thermal runaway propagation rates are calculated based on the battery thickness and the thermal propagation time. The propagation rate for the sodium-ion battery is 1.726 mm/s, for the LFP battery is 1.241 mm/s, for the NCM523 battery is 3.375 mm/s, and for the NCM622 battery is 2.7 mm/s. The propagation rates from largest to smallest are: NCM523 > NCM622 > NIBs > LFP. The LFP battery exhibits the lowest thermal runaway propagation rate, attributed to the lower thermal reactivity of the LiFePO₄ material. The slower internal chemical reaction rates compared to NCM and sodium-ion batteries contribute to its reduced propagation speed.

Figure 7b Heat generated by the heating plate and the duration of heating of the electric heating plate. According to Equation (2):

$$Q = Pt_Q \quad (2)$$

where Q represents the heat generated by the heating plate (kJ), P is the power of the heating plate (400 W), and t_Q is the duration of heating (s). The heating durations were 394 s for the sodium-ion battery, 1482 s for the LFP battery, 685 s for the NCM523 battery, and 656 s for the NCM622 battery.

Using Equation (2), the heat generated by the heating plate (Q) can be calculated. If we neglect the thermal capacity of the heating plate itself and the heat lost to the environment (since one side of the heating plate is insulated with a mica sheet and the other side is in direct contact with the battery surface, the heat loss to the environment is minimal), the heat generated by the heating plate (Q) can be approximated as the heat injected into the battery. The heat injected into the batteries is as follows: 592.8 kJ for the LFP battery, 274 kJ for the NCM523 battery, and 262 kJ for the NCM622 battery. A higher value of Q indicates that thermal runaway in the battery is more difficult to trigger. The heat input to the batteries, from largest to smallest, is: LFP > NCM622 > NCM523 > NIBs. The NIBs battery has the lowest triggering energy for thermal runaway, while the LFP battery has the highest triggering energy, making it the safest.

3.2. Mass Loss During Battery Thermal Runaway

During the thermal runaway process, the mass loss rate is a key indicator for assessing the severity of battery thermal runaway. In this study, thermal runaway was triggered through lateral heating. When the safety valve reached its critical pressure, it opened, causing intense reactions between the electrolyte and electrode materials inside the battery. This resulted in the production of large quantities of high-temperature, high-pressure gas-liquid mixtures, accompanied by the ejection of substantial thermal runaway reaction products and internal battery materials [16].

As shown in Figure 8a–e the ejected products from the sodium-ion battery (NIBs) and the lithium iron phosphate battery (LFP) during thermal runaway are primarily liquid substances, with the electrolyte being the main component. In contrast, the ejected products from the NCM batteries (NCM523 and NCM622) are primarily black solids, consisting mainly of cathode materials, anode materials, and chemical reaction products.

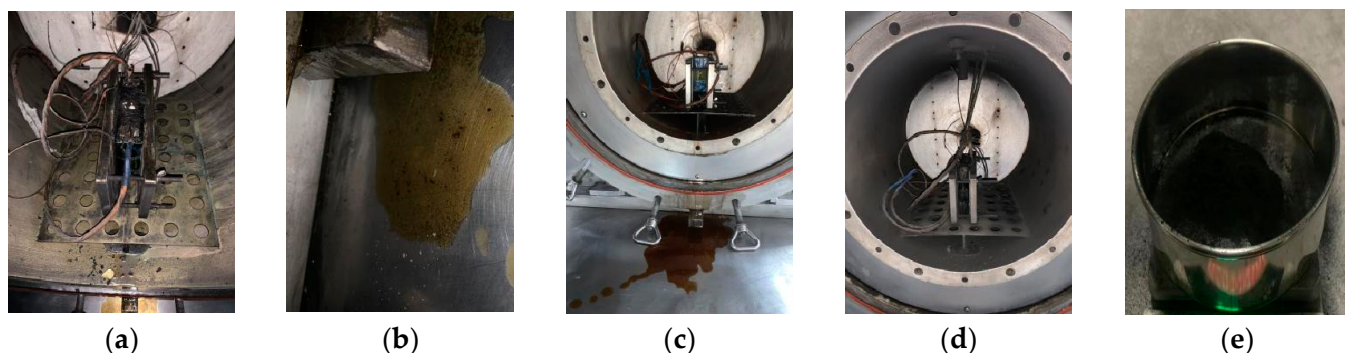


Figure 8. Liquid and Solid Ejected Products After Thermal Runaway of Four Batteries. (a) Post-thermal runaway state of the sodium-ion battery. (b) Liquid ejected products from the sodium-ion battery after thermal runaway. (c) Liquid ejected products from the LFP battery after thermal runaway. (d) Post-thermal runaway state of the NCM battery. (e) Solid ejected products collected from the NCM battery after thermal runaway.

As shown in Figure 9a, the initial mass (m_0) and the post-experiment mass of the battery remnants (m_1) were measured for the four batteries. The mass loss rate was calculated using Equation (3):

$$\varphi_{loss} = \frac{m_0 - m_1}{m_0} \times 100\% \quad (3)$$

where ϕ_{loss} represents the mass loss rate (%), m_0 is the initial mass of the battery (g), and m_1 is the mass of the battery remnants (g).

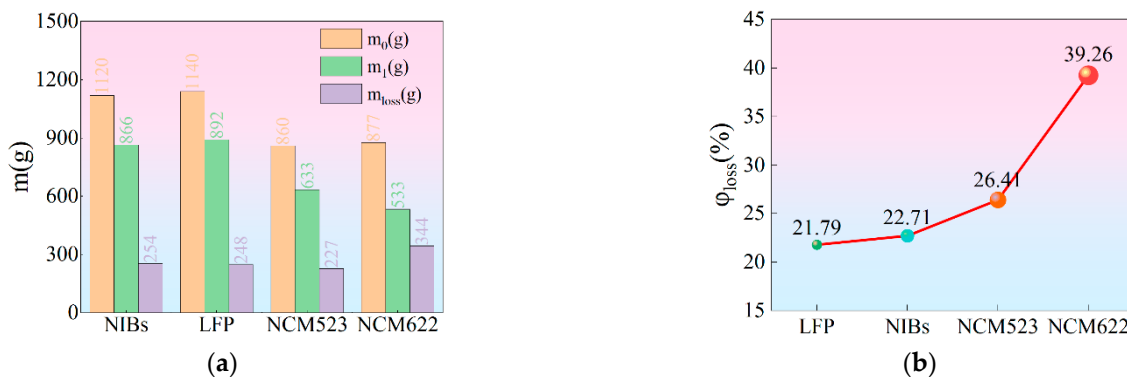


Figure 9. Battery Mass Before and After Thermal Runaway. (a) Mass and mass loss of four batteries before and after thermal runaway. (b) Mass loss rate of four batteries after thermal runaway.

Using Equation (3), the mass loss rates for the four batteries were calculated based on the initial mass of new batteries and the post-thermal runaway remnant mass. As shown in Figure 9b, the mass loss rates for the lithium iron phosphate (LFP) battery, sodium-ion (NIBs) battery, NCM523 lithium battery, and NCM622 lithium battery were 21.79%, 22.71%, 26.41%, and 39.26%, respectively.

Due to differences in the severity of thermal runaway and the type of ejected materials, the mass loss rates of the NCM523, NCM622, and NIBs batteries were higher than that of the LFP battery. The NCM622 battery, with its high energy density, ejected a significant amount of internal rolled material during thermal runaway, resulting in a much higher mass loss rate compared to the other three samples. The mass loss rate of the NIBs battery was slightly higher than that of the LFP battery, indicating that the thermal runaway characteristics of mass loss for NIBs and LFP are relatively similar.

Based on the above analysis, if the mass loss rate is used as an indicator to evaluate the severity of thermal runaway ejection, the NCM batteries exhibit significantly more violent ejection behavior compared to LFP and NIBs batteries. Among the four types, the LFP battery showed the least violent ejection behavior.

3.3. Gas Composition and Constituents from Battery Thermal Runaway

During the thermal runaway process, the thermal stability of internal materials such as the cathode, anode, electrolyte, and separator plays a critical role in determining the battery's thermal runaway threshold. Research indicates that lithium-ion batteries produce significant amounts of toxic and flammable gases during thermal runaway [19].

In this study, thermal runaway was triggered for four types of batteries in an N_2 environment. The generated gases were collected and analyzed using gas chromatography (GC). The results show that the primary gas components produced during thermal runaway are carbon dioxide (CO_2), hydrogen (H_2), carbon monoxide (CO), methane (CH_4), ethylene (C_2H_4), propylene (C_3H_6), ethane (C_2H_6), and trace hydrocarbons. Although the cathode materials vary between battery types, the types of gases generated during thermal runaway are largely similar. This is because the decomposition of different cathode materials at various temperatures produces different concentrations of oxygen (O_2), which reacts with the electrolyte to release other gases.

The insertion of lithium or sodium into the anode material is also a critical factor affecting the types of gases produced. Additionally, the reaction between the electrolyte and the anode at high temperatures generates a large volume of gas and heat [20,21].

Figure 10 shows the gas composition and proportions produced by the four batteries during thermal runaway in an N₂ environment.

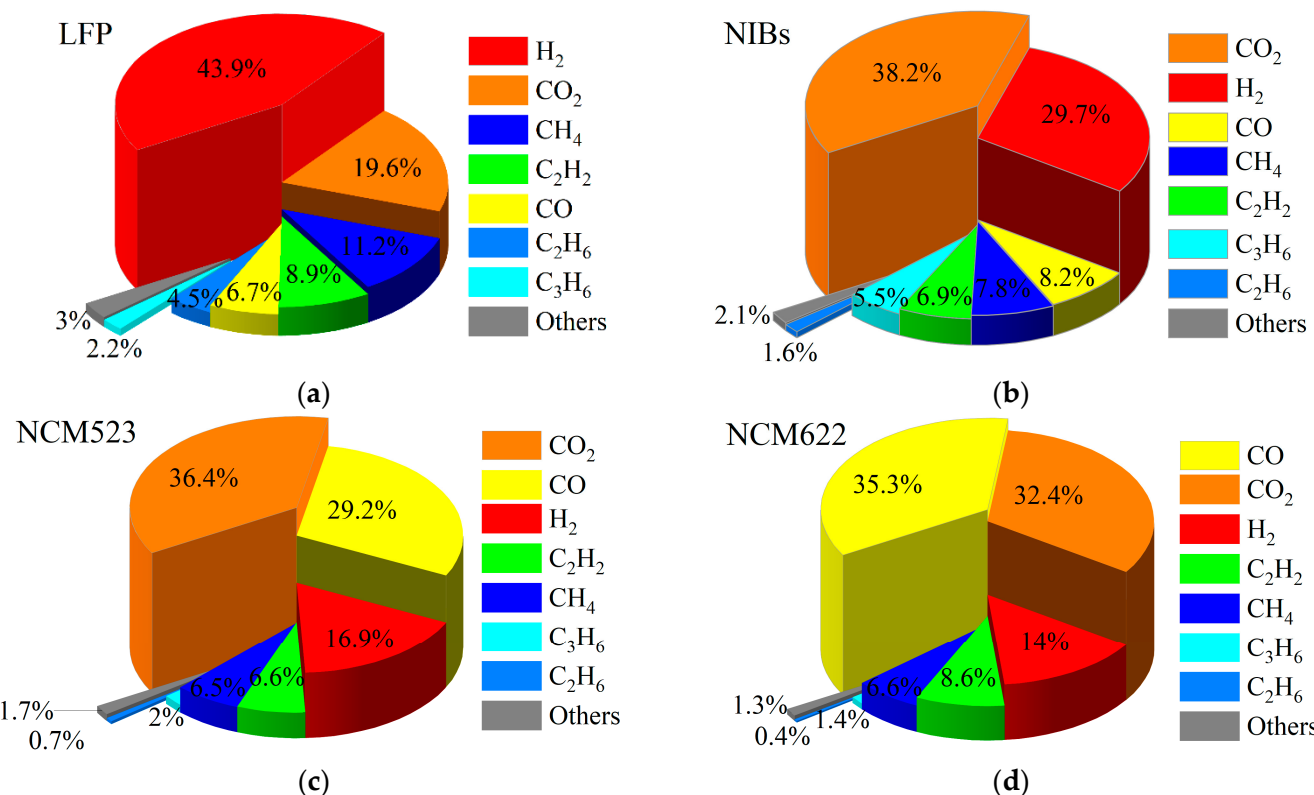
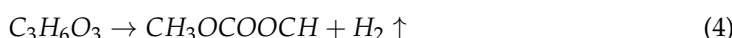


Figure 10. Gas Composition After Thermal Runaway of Four Batteries in an N₂ Atmosphere. (a) Gas composition after thermal runaway of the LFP battery. (b) Gas composition after thermal runaway of the NIBs battery. (c) Gas composition after thermal runaway of the NCM523 battery. (d) Gas composition after thermal runaway of the NCM622 battery.

Figure 10a presents the gas composition data for the LFP battery. The gases with a volume fraction exceeding 6% are as follows: H₂ (43.9%) > CO₂ (19.6%) > CH₄ (11.2%) > C₂H₂ (8.9%) > CO (6.7%). H₂ is the most abundant component, primarily because the LFP cathode material has an olivine crystal structure with excellent thermal stability. At higher temperatures, the organic solvents and additives in the electrolyte decompose, producing large amounts of H₂. The reaction mechanism is as follows [22–26]:

At temperatures above 200 °C, organic solvents begin to decompose.



When the temperature exceeds 230 °C, the graphite anode decomposes, and lithium (Li) directly contacts the electrolyte and binder. At temperatures above 260 °C, the binders polyvinylidene fluoride (PVDF) and carboxymethyl cellulose (CMC) start to decompose and react with lithium (Li):

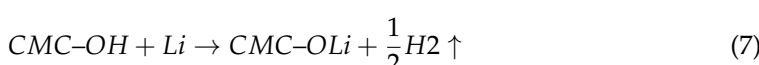
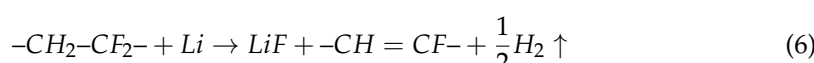
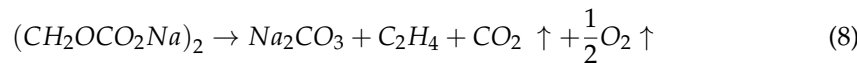
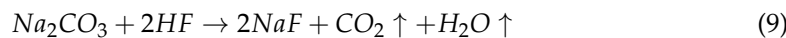


Figure 10b shows the gas composition data for the sodium-ion battery during thermal runaway. The gases with a volume fraction exceeding 6% are as follows: CO_2 (38.2%) > H_2 (29.7%) > CO (8.2%) > CH_4 (7.8%) > C_2H_2 (6.9%). Among these, CO_2 is the most abundant component. The mechanism for CO_2 generation is as follows [23–27]:

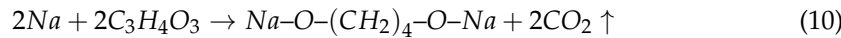
When the temperature reaches 90–110 °C, the Solid Electrolyte Interface (SEI) layer begins to decompose:



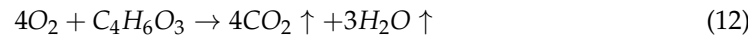
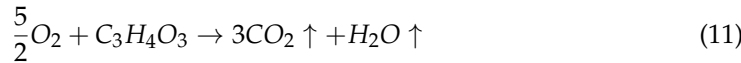
When the temperature reaches 120 °C, the Charging Electrolyte Interface (CEI) layer begins to decompose:



When the temperature reaches 220 °C, the SEI layer and CEI layer continue to decompose, and the battery anode undergoes intense redox reactions with the organic solvents, generating large amounts of CO_2 :



At temperatures above 200 °C, the cathode material of the sodium-ion battery decomposes, releasing O_2 , which reacts with the electrolyte solvent to generate large amounts of CO_2 gas:



The incomplete combustion of the graphite material in the anode of the sodium-ion battery also generates large amounts of CO_2 :

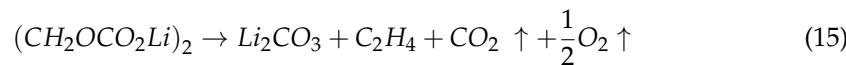


The combustible gases produced by side reactions in sodium-ion batteries generate large amounts of CO_2 during complete combustion in an oxygen-rich environment:

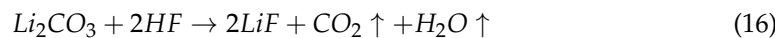


Figure 10c shows the gas composition data for the NCM523 battery during thermal runaway. The gases with a volume fraction exceeding 6% are as follows: CO_2 (36.4%) > CO (29.2%) > H_2 (16.9%) > C_2H_2 (6.6%) > CH_4 (6.5%). Among these, CO_2 is the most abundant component. The mechanism for CO_2 generation is as follows [23–26,28]:

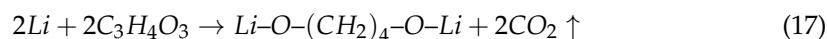
When the temperature reaches 90–110 °C, the Solid Electrolyte Interface (SEI) layer begins to decompose:



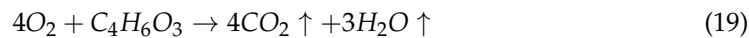
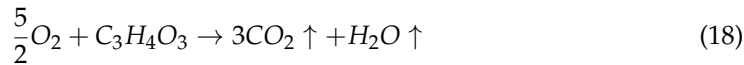
When the temperature reaches 120 °C, the Charging Electrolyte Interface (CEI) layer begins to decompose:



When the temperature reaches 220 °C, the SEI layer and CEI layer continue to decompose, and the anode of the NCM523 battery undergoes intense redox reactions with the organic solvents, generating large amounts of CO₂:



At temperatures above 200 °C, the cathode material of the NCM523 battery decomposes, releasing O₂, which reacts with the electrolyte solvent to generate large amounts of CO₂ gas:



The incomplete combustion of the graphite material in the anode of the NCM523 battery also generates large amounts of CO₂:



The combustible gases produced by side reactions in the NCM523 battery, when completely combusted with the O₂ released from the decomposition of the cathode material, generate large amounts of CO₂:

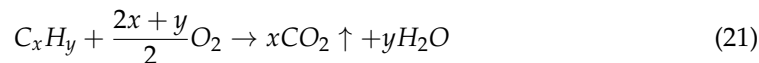
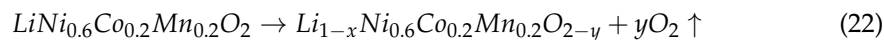
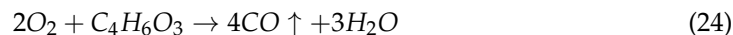
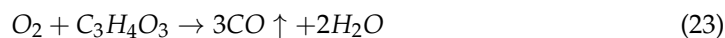


Figure 10d shows the gas composition data for the NCM622 battery during thermal runaway. The gases with a volume fraction exceeding 6% are as follows: CO (35.3%) > CO₂ (32.4%) > H₂ (14%) > C₂H₂ (8.6%) > CH₄ (6.6%). Among these, CO is the most abundant gas. The mechanism for CO generation is as follows [23–26,29–31]:

The cathode of the NCM622 battery decomposes under heat, releasing large amounts of oxygen:



At high temperatures, the O₂ released from the decomposition of the NCM622 cathode reacts with the electrolyte solvent, generating large amounts of CO:



The incomplete combustion of the anode in the NCM622 battery generates large amounts of CO:



The combustible gases produced by side reactions in the NCM622 battery, when incompletely combusted with the O₂ released from the decomposition of the cathode material, generate large amounts of CO:

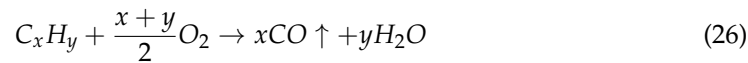


Figure 11 presents the normalized gas volume data from the thermal runaway of four types of batteries. It was observed that the gas components with a volume fraction

difference exceeding 5% among the four batteries are limited to three gases: CO, H₂, and CO₂.

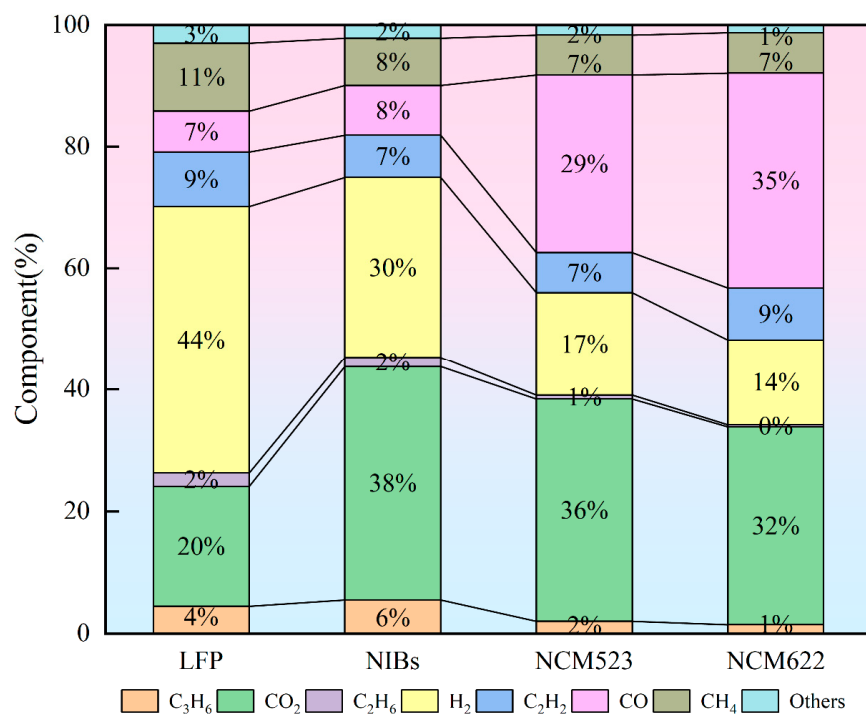


Figure 11. Normalized Gas Composition Comparison for Thermal Runaway of Four Batteries.

The volume fraction of CO is as follows: NCM622 (35%) > NCM523 (29%) > NIBs (8%) > LFP (7%). The cathode materials of NCM622 and NCM523 contain higher nickel content, which makes the cathode more prone to redox reactions (Ni³⁺ reduced to Ni²⁺) during thermal runaway. These reactions generate large amounts of oxygen, which further reacts with the decomposition products of the electrolyte at high temperatures to produce significant CO [32,33]. NCM622, with a higher nickel content than NCM523, exhibits lower stability and releases more oxygen, leading to a higher CO yield. The cathode material of NIBs, a layered sodium oxide, is more thermally stable than NCM batteries, releasing less oxygen and thus producing less CO from reactions with electrolyte decomposition products. LFP, with its olivine crystal structure, exhibits the highest stability and releases the least amount of oxygen during thermal runaway. Consequently, the decomposition of the electrolyte is minimal, resulting in the lowest CO yield among the four batteries [23,34].

The volume fraction of H₂ is as follows: LFP (44%) > NIBs (30%) > NCM523 (17%) > NCM622 (14%). LFP has the highest H₂ content (44%) because its stable cathode material decomposes less and releases minimal oxygen. Consequently, the carbonate-based electrolytes (e.g., EC, DMC) primarily undergo self-decomposition at high temperatures, generating large amounts of hydrogen. In NCM batteries, the cathode material decomposes easily at high temperatures, releasing significant oxygen, which reacts with the electrolyte to generate CO and CO₂. This results in relatively lower H₂ production. NCM622, with higher nickel content and reactivity than NCM523, produces even less H₂. Sodium-ion batteries (NIBs) have better thermal stability than high-nickel NCM batteries but are less stable than LFP, placing their H₂ production between the two extremes [23,34,35].

The volume fraction of CO₂ is as follows: NIBs (38%) > NCM523 (36%) > NCM622 (32%) > LFP (20%). NIBs generate the most CO₂ during thermal runaway because their cathode material, a layered sodium oxide, releases sufficient oxygen to react with the electrolyte and produce large amounts of CO₂, even though the oxygen release is less than that of NCM batteries. NCM523 and NCM622, both high-nickel NCM batteries, generate

CO_2 at 36% and 32%, respectively. The CO_2 yields are comparable because the NCM cathode material releases large amounts of oxygen during thermal runaway, which reacts with the carbonate solvents in the electrolyte to form CO_2 . However, the increased oxygen release also promotes the formation of CO, partially offsetting the generation of CO_2 . As a result, although NCM622 releases more oxygen, its CO_2 yield is slightly lower than NCM523. LFP, with its highly stable LiFePO_4 cathode, releases minimal oxygen, resulting in weak oxidative reactions with the electrolyte. The decomposition of the electrolyte in LFP is primarily due to pyrolysis rather than oxidation, leading to the lowest CO_2 yield during thermal runaway [23,25,36,37].

3.4. Flammability Limits of Gases Produced During Battery Thermal Runaway

Based on the gas composition analysis, the flammability limits (lower and upper limits) of the mixed gases produced during the thermal runaway of the four batteries were calculated using Le Chatelier's Equations (27) and (28) [38–40].

$$\text{LFL}_{\text{mix}} = \frac{1 - C_{\text{inert}}}{\sum \frac{C_i}{\text{LFL}_i}} \quad (27)$$

$$\text{UFL}_{\text{mix}} = \frac{1 - C_{\text{inert}}}{\sum \frac{C_i}{\text{UFL}_i}} \quad (28)$$

In the equations, LFL_{mix} represents the lower flammability limit (LFL) of the mixed gases produced after battery thermal runaway (TR). C_{inert} represents the volume fraction of non-combustible gases, C_i represents the percentage of gas i in the mixture, and LFL_i represents the lower flammability limit of gas i . Similarly, UFL_{mix} represents the upper flammability limit (UFL) of the mixed gases, and UFL_i represents the upper flammability limit of gas i .

Figure 12a presents the flammability limits of individual gases from the literature. These values were substituted into the equations to calculate the UFL and LFL of the mixed gases produced by the four batteries, as shown in Figure 12b.

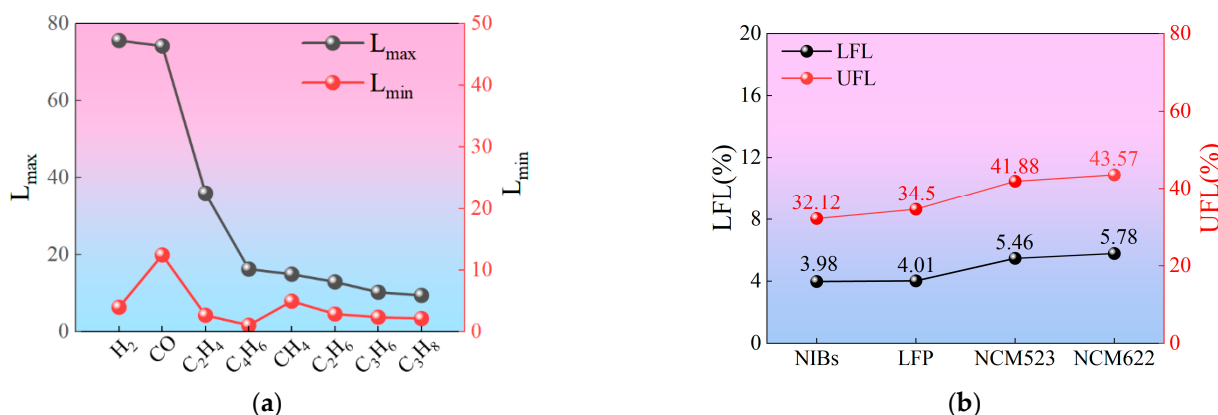


Figure 12. Flammability Range of Gases Produced During Thermal Runaway of Four Batteries. (a) Flammability limit data of individual gases. (b) Flammability limits of mixed gases for the four batteries.

It was found that the sodium-ion battery had the lower flammability limit, with an LFL value of 3.98. This is primarily because the gases produced during the thermal runaway of the sodium-ion battery contain a significant amount of propylene (C_3H_6), which has the lower flammability limit. Consequently, the mixed gases from the sodium-ion battery exhibit the lower flammability limit, resulting in the highest explosion hazard.

By comparing the flammability limits, the ranking of lower flammability limits (LFL_{mix}) from highest to lowest is: NIBs > LFP > NCM622 > NCM523. Therefore, sodium-ion batteries present the highest explosion risk.

According to the study by Li et al., the combustible range (R_F) and the combustible hazard index (H_F) are defined to assess the hazard of combustible gases generated during battery thermal runaway [37]. The calculation formulas are shown in Equations (29) and (30), and the calculation results are presented in the table below.

$$R_F = UFL - LFL \quad (29)$$

$$H_F = \frac{UFL - LFL}{LFL} \times 100\% \quad (30)$$

As shown in Table 2, the combustible range (R_F) of the gases produced during thermal runaway of the four types of batteries decreases in the following order: NCM622 > NCM523 > LFP > NIBs. However, the hazard index (H_F) shows the opposite order compared to the combustible range (R_F). This is because a lower lower flammability limit (LFL) can result in a higher H_F . Even though the combustible range is larger, the relatively lower LFL increases the hazard index, leading to a higher risk despite the wider combustible range.

Table 2. Combustible Range (R_F) and Combustible Hazard Index (H_F) for Four Types of Batteries.

Type	LFL	UFL	R_F	H_F
NIBs	3.39	32.12	28.73	8.474926
LFP	4.01	34.5	30.49	7.603491
NCM523	5.46	41.88	36.42	6.67033
NCM622	5.78	43.57	37.79	6.538062

4. Conclusions and Summary

This study conducted thermal runaway experiments in a nitrogen environment using a custom-sealed container. Four 50 Ah batteries were tested, with thermal runaway triggered by lateral heating using a 400 W heating plate. Data on the surface temperature, voltage changes, and mass loss were collected, and gas chromatography (GC) was used to analyze the gas composition during thermal runaway (TR). The following conclusions were drawn:

- (1) The sodium-ion battery (NIBs) and lithium iron phosphate battery (LFP) first triggered their safety valves to release gases during the initial ejection phase, followed by a period of heat accumulation (251 s for NIBs and 453 s for LFP) before entering the intense thermal runaway ejection phase. In contrast, for NCM622 and NCM523 batteries, the opening of the safety valve and the onset of thermal runaway occurred almost simultaneously. The critical surface temperatures on the heated side (T_{f-TR}) were as follows: LFP (346 °C) > NIBs (292 °C) > NCM523 (290 °C) > NCM622 (281 °C). LFP batteries exhibited the highest thermal runaway critical temperature. The heat input (Q) required to trigger thermal runaway was: LFP (592.8 kJ) > NCM622 (262 kJ) > NCM523 (274 kJ) > NIBs (158 kJ). NIBs batteries required the least energy to trigger thermal runaway, while LFP batteries required the most.
- (2) During thermal runaway, NCM523 and NCM622 batteries released gases and black solid particles, with mass losses of 26.41% and 39.26%, respectively. LFP batteries primarily ejected liquid electrolytes and byproduct gases, with a mass loss of 21.79%. The ejected materials of NIBs batteries were similar to those of LFP batteries, with a mass loss of 22.71%. NCM batteries exhibited significantly greater mass loss compared to LFP and NIBs batteries.
- (3) The main gases produced during thermal runaway were carbon dioxide (CO₂), hydrogen (H₂), carbon monoxide (CO), methane (CH₄), ethylene (C₂H₄), propylene (C₃H₆),

ethane (C_2H_6), and other trace hydrocarbons. The most variable flammable gases were CO and H₂. The CO content ranked as follows: NCM622 (35%) > NCM523 (29%) > NIBs (8%) > LFP (7%). The H₂ content ranked as follows: LFP (44%) > NIBs (30%) > NCM523 (17%) > NCM622 (14%). NIBs had the lowest LFL and highest R_F, indicating the highest explosion risk.

These conclusions provide valuable insights for battery selection and design in energy storage applications.

Author Contributions: Conceptualization, C.Q. and H.W.; methodology, C.Q., M.L. and C.L.; software, C.Q., Y.L. and C.S.; validation, H.W., M.L. and N.W.; formal analysis, C.Q.; investigation, C.Q.; resources, H.W.; data curation, C.Q.; writing—original draft preparation, C.Q.; writing—review and editing, C.Q., Y.L., M.L. and H.W.; visualization, C.Q., C.L., H.Z. and Y.W.; supervision, H.W., M.L. and Y.L.; project administration, H.W., M.L. and Y.L.; funding acquisition, H.W. All authors have read and agreed to the published version of the manuscript.

Funding: This research is generously supported by Carbon Neutrality and Energy System Transformation (CNEST) Program, the National Natural Science Foundation of China for the Youth Project (No. 52207240, No. 52207241, and No. 52406253), Key R&D Program of Shandong Province, China and Development Major Science and Technology Innovation Project of Shandong Province (No. 2024CXGC010806), the Youth Project of the Natural Science Foundation of Shandong Province (No. ZR2022QE099), the Youth and Excellence Team Reward Scheme of Shandong Province (No. 2023KJ323). The authors gratefully acknowledge the financial support from the Joint Science Foundation of Guangdong Province (Grant No. 21201910260000023).

Data Availability Statement: The data is available through appropriate requests.

Conflicts of Interest: The authors declare no conflict of interest.

References

1. Kong, D.; Lv, H.; Ping, P.; Wang, G. A review of early warning methods of thermal runaway of lithium ion batteries. *J. Energy Storage* **2023**, *64*, 107073. [[CrossRef](#)]
2. Shahid, S.; Agelin-Chaab, M. A review of thermal runaway prevention and mitigation strategies for lithium-ion batteries. *Energy Convers. Manag. X* **2022**, *16*, 100310. [[CrossRef](#)]
3. Zhu, M.; Yao, J.; Qian, F.; Luo, W.; Chen, Y.; Zhao, L.; Chen, M. Study on Thermal Runaway Propagation Characteristics of Lithium Iron Phosphate Battery Pack under Different SOCs. *Electronics* **2023**, *12*, 200. [[CrossRef](#)]
4. Galushkin, N.; Yazvinskaya, N.; Galushkin, D. Mechanism of thermal runaway in lithium-ion cells. *J. Electrochem. Soc.* **2018**, *165*, A1303. [[CrossRef](#)]
5. Liao, Z.; Zhang, S.; Li, K.; Zhang, G.; Habetler, T.G. A survey of methods for monitoring and detecting thermal runaway of lithium-ion batteries. *J. Power Sources* **2019**, *436*, 226879. [[CrossRef](#)]
6. Song, L.; Zheng, Y.; Xiao, Z.; Wang, C.; Long, T. Review on thermal runaway of lithium-ion batteries for electric vehicles. *J. Electron. Mater.* **2022**, *51*, 30–46. [[CrossRef](#)]
7. Hu, D.; Huang, S.; Wen, Z.; Gu, X.; Lu, J. A review on thermal runaway warning technology for lithium-ion batteries. *Renew. Sustain. Energy Rev.* **2024**, *206*, 114882. [[CrossRef](#)]
8. Xu, L.; Wang, S.; Li, Y.; Li, Y.; Sun, J.; Zhao, F.; Wang, H.; Wang, Y.; Xu, C.; Feng, X. Thermal runaway propagation behavior and gas production characteristics of NCM622 battery modules at different state of charge. *Process Saf. Environ. Prot.* **2024**, *185*, 267–276. [[CrossRef](#)]
9. Qi, C.; Liu, Z.; Lin, C.; Liu, X.; Liu, D.; Li, Z.; Yi, A. The gas production characteristics and catastrophic hazards evaluation of thermal runaway for $LiNi_{0.5}Co_{0.2}Mn_{0.3}O_2$ lithium-ion batteries under different SOCs. *J. Energy Storage* **2024**, *88*, 111678. [[CrossRef](#)]
10. Zou, K.; He, K.; Lu, S. Venting composition and rate of large-format $LiNi_{0.8}Co_{0.1}Mn_{0.1}O_2$ pouch power battery during thermal runaway. *Int. J. Heat Mass Transf.* **2022**, *195*, 123133. [[CrossRef](#)]
11. Jia, Z.; Wang, S.; Qin, P.; Li, C.; Jin, K.; Sun, J.; Wang, Q. Investigation of gas diffusion behavior and detection of 86 Ah LiFePO₄ batteries in energy storage systems during thermal runaway. *Process Saf. Environ. Prot.* **2024**, *184*, 579–588. [[CrossRef](#)]

12. Wang, K.; Wu, D.; Chang, C.; Zhang, J.; Ouyang, D.; Qian, X. Charging rate effect on overcharge-induced thermal runaway characteristics and gas venting behaviors for commercial lithium iron phosphate batteries. *J. Clean. Prod.* **2024**, *434*, 139992. [[CrossRef](#)]
13. Cui, Y.; Shi, D.; Wang, Z.; Mou, L.; Ou, M.; Fan, T.; Bi, S.; Zhang, X.; Yu, Z.; Fang, Y. Thermal Runaway Early Warning and Risk Estimation Based on Gas Production Characteristics of Different Types of Lithium-Ion Batteries. *Batteries* **2023**, *9*, 438. [[CrossRef](#)]
14. Lin, C.; Yan, H.; Qi, C.; Liu, Z.; Liu, D.; Liu, X.; Lao, L.; Li, Z.; Sun, Y. Thermal runaway and gas production characteristics of semi-solid electrolyte and liquid electrolyte lithium-Ion batteries: A comparative study. *Process Saf. Environ. Prot.* **2024**, *189*, 577–586. [[CrossRef](#)]
15. Bordes, A.; Marlair, G.; Zantman, A.; Chesnaye, A.; Lore, P.-A.L.; Lecocq, A. Safety evaluation of a sodium-ion cell: Assessment of vent gas emissions under thermal runaway. *ACS Energy Lett.* **2022**, *7*, 3386–3391. [[CrossRef](#)]
16. Wang, K.; Ouyang, D.; Qian, X.; Yuan, S.; Chang, C.; Zhang, J.; Liu, Y. Early warning method and fire extinguishing technology of lithium-ion battery thermal runaway: A review. *Energies* **2023**, *16*, 2960. [[CrossRef](#)]
17. Peng, Y.; Wang, H.; Jin, C.; Huang, W.; Zhang, F.; Li, B.; Ju, W.; Xu, C.; Feng, X.; Ouyang, M. Thermal runaway induced gas hazard for cell-to-pack (CTP) lithium-ion battery pack. *J. Energy Storage* **2023**, *72*, 108324. [[CrossRef](#)]
18. Lyu, P.; Liu, X.; Qu, J.; Zhao, J.; Huo, Y.; Qu, Z.; Rao, Z. Recent advances of thermal safety of lithium ion battery for energy storage. *Energy Storage Mater.* **2020**, *31*, 195–220. [[CrossRef](#)]
19. Feng, X.; Ouyang, M.; Liu, X.; Lu, L.; Xia, Y.; He, X. Thermal runaway mechanism of lithium ion battery for electric vehicles: A review. *Energy Storage Mater.* **2018**, *10*, 246–267. [[CrossRef](#)]
20. Koch, S.; Fill, A.; Birke, K.P. Comprehensive gas analysis on large scale automotive lithium-ion cells in thermal runaway. *J. Power Sources* **2018**, *398*, 106–112. [[CrossRef](#)]
21. Spotte-Smith, E.W.C.; Blau, S.M.; Barter, D.; Leon, N.J.; Hahn, N.T.; Redkar, N.S.; Zavadil, K.R.; Liao, C.; Persson, K.A. Chemical reaction networks explain gas evolution mechanisms in mg-ion batteries. *J. Am. Chem. Soc.* **2023**, *145*, 12181–12192. [[CrossRef](#)] [[PubMed](#)]
22. Kumai, K.; Miyashiro, H.; Kobayashi, Y.; Takei, K.; Ishikawa, R. Gas generation mechanism due to electrolyte decomposition in commercial lithium-ion cell. *J. Power Sources* **1999**, *81*, 715–719. [[CrossRef](#)]
23. Sharifi-Asl, S.; Lu, J.; Amine, K.; Shahbazian-Yassar, R. Oxygen release degradation in Li-ion battery cathode materials: Mechanisms and mitigating approaches. *Adv. Energy Mater.* **2019**, *9*, 1900551. [[CrossRef](#)]
24. Wei, G.; Huang, R.; Zhang, G.; Jiang, B.; Zhu, J.; Guo, Y.; Han, G.; Wei, X.; Dai, H. A comprehensive insight into the thermal runaway issues in the view of lithium-ion battery intrinsic safety performance and venting gas explosion hazards. *Appl. Energy* **2023**, *349*, 121651. [[CrossRef](#)]
25. Li, J.; Li, Y.; Zeng, W. Gas sensing technology as the key to safety warning of lithium-ion battery: Recent advance. *Sens. Actuators A Phys.* **2023**, *365*, 114890. [[CrossRef](#)]
26. Qiu, M.; Liu, J.; Cong, B.; Cui, Y. Research progress in thermal runaway vent gas characteristics of li-ion battery. *Batteries* **2023**, *9*, 411. [[CrossRef](#)]
27. Zhou, Q.; Li, Y.; Tang, F.; Li, K.; Rong, X.; Lu, Y.; Chen, L.; Hu, Y.-S. Thermal stability of high power 26650-type cylindrical Na-ion batteries. *Chin. Phys. Lett.* **2021**, *38*, 076501. [[CrossRef](#)]
28. Rowden, B.; Garcia-Araez, N. A review of gas evolution in lithium ion batteries. *Energy Rep.* **2020**, *6*, 10–18. [[CrossRef](#)]
29. Kim, Y. Mechanism of gas evolution from the cathode of lithium-ion batteries at the initial stage of high-temperature storage. *J. Mater. Sci.* **2013**, *48*, 8547–8551. [[CrossRef](#)]
30. Zhang, S.S. Insight into the gassing problem of Li-ion battery. *Front. Energy Res.* **2014**, *2*, 59. [[CrossRef](#)]
31. Qi, C.; Liu, Z.; Lin, C.; Hu, Y. Review of Gas Generation Behavior during Thermal Runaway of Lithium-Ion Batteries. *SAE Int. J. Electrified Veh.* **2023**, *13*, 399–413. [[CrossRef](#)]
32. Ma, B.; Liu, J.; Yu, R. Study on the flammability limits of lithium-ion battery vent gas under different initial conditions. *ACS Omega* **2020**, *5*, 28096–28107. [[CrossRef](#)]
33. Berkes, B.B.; Schiele, A.; Sommer, H.; Brezesinski, T.; Janek, J. On the gassing behavior of lithium-ion batteries with NCM523 cathodes. *J. Solid State Electrochem.* **2016**, *20*, 2961–2967. [[CrossRef](#)]
34. Somandepalli, V.; Marr, K.; Horn, Q. Quantification of combustion hazards of thermal runaway failures in lithium-ion batteries. *SAE Int. J. Altern. Powertrains* **2014**, *3*, 98–104. [[CrossRef](#)]
35. Lyu, S.; Li, N.; Sun, L.; Jiao, S.; Chen, H.; Song, W.-L. Rapid operando gas monitor for commercial lithium ion batteries: Gas evolution and relation with electrode materials. *J. Energy Chem.* **2022**, *72*, 14–25. [[CrossRef](#)]
36. Wang, Z.; Zhu, L.; Liu, J.; Wang, J.; Yan, W. Gas sensing technology for the detection and early warning of battery thermal runaway: A review. *Energy Fuels* **2022**, *36*, 6038–6057. [[CrossRef](#)]
37. Li, W.; Wang, H.; Zhang, Y.; Ouyang, M. Flammability characteristics of the battery vent gas: A case of NCA and LFP lithium-ion batteries during external heating abuse. *J. Energy Storage* **2019**, *24*, 100775. [[CrossRef](#)]

38. Zhang, Q.; Liu, T.; Hao, C.; Qu, Y.; Niu, J.; Wang, Q.; Chen, D. In situ Raman investigation on gas components and explosion risk of thermal runaway emission from lithium-ion battery. *J. Energy Storage* **2022**, *56*, 105905. [[CrossRef](#)]
39. Zhang, Q.; Niu, J.; Yang, J.; Liu, T.; Bao, F.; Wang, Q. In-situ explosion limit analysis and hazards research of vent gas from lithium-ion battery thermal runaway. *J. Energy Storage* **2022**, *56*, 106146. [[CrossRef](#)]
40. Wang, J.; Wang, L.; Liu, J.; Wang, Z.; Fei, B.; Zhu, C.; Pan, R.; Zhou, X. Investigation of gas explosion hazards and characteristics during overcharged behavior of nickel-cobalt-manganese (523) lithium-ion battery. *J. Energy Storage* **2024**, *86*, 111436. [[CrossRef](#)]

Disclaimer/Publisher’s Note: The statements, opinions and data contained in all publications are solely those of the individual author(s) and contributor(s) and not of MDPI and/or the editor(s). MDPI and/or the editor(s) disclaim responsibility for any injury to people or property resulting from any ideas, methods, instructions or products referred to in the content.